Complete microviscosity maps of living plant cells and tissues with a toolbox of targeting mechanoprobes

Lucile Michels[a] , Vera Gorelova[b], Yosapol Harnvanichvech[a,b] , Jan Willem Borst[b], Bauke Albada[c] , Dolf Weijers[b,1] , and Joris Sprakel[a,1]

[a]Physical Chemistry and Soft Matter, Wageningen University & Research, 6708 WE Wageningen, The Netherlands; [b]Laboratory of Biochemistry, Wageningen University & Research, 6708 WE Wageningen, The Netherlands; and [c]Laboratory of Organic Chemistry, Wageningen University & Research, 6708 WE Wageningen, The Netherlands

Mechanical patterns control a variety of biological processes in plants. The microviscosity of cellular structures effects the diffusion rate of molecules and organelles, thereby affecting processes such as metabolism and signaling. Spatial variations in local viscosity are also generated during fundamental events in the cell life cycle. While crucial to a complete understanding of plant mechanobiology, resolving subcellular microviscosity patterns in plants has remained an unsolved challenge. We present an imaging microviscosimetry toolbox of molecular rotors that yield complete microviscosity maps of cells and tissues, specifically targeting the cytosol, vacuole, plasma membrane, and wall of plant cells. These boron-dipyrromethene (BODIPY)-based molecular rotors are rigidochromic by means of coupling the rate of an intramolecular rotation, which depends on the mechanics of their direct surroundings, with their fluorescence lifetime. This enables the optical mapping of fluidity and porosity patterns in targeted cellular compartments. We show how apparent viscosity relates to cell function in the root, how the growth of cellular protrusions induces local tension, and how the cell wall is adapted to perform actuation surrounding leaf pores. These results pave the way to the noninvasive micromechanical mapping of complex tissues.

molecular rotors | microviscosity | FLIM | plant mechanobiology

The functioning and development of organisms are generally described by gene expression and interactions between proteins and signaling molecules. Although this chemistry-centered view on the processes of life has provided tremendous insight in the inner workings of living systems, it is becoming clear that mechanical forces also play an important role in biological systems. There are no generalized concepts yet that explain how molecular interactions intertwine with mechanical forces across the kingdoms of life. Therefore, at present, mechanical and chemical influences on living systems are mostly disconnected. Single-molecule methods have generated deep insights into the mechanical response of individual molecules or molecular assemblies. Nevertheless, mapping mechanical patterns in vivo, from the subcellular scale up to that of multicellular tissues, remains a daunting challenge. One mechanical property of particular importance is the microviscosity of subcellular structures and spaces. Microviscosity determines the diffusion rates of all molecules and organelles within a cell, thereby impacting cellular metabolism (1) and processes such as signaling and enzymatic reactions (2, 3). Spatial gradients in local viscosity can also be actively generated by cells during important stages of the life cycle, such as polarization, division, or differentiation (4–9). In plants, cells are mechanically confined by and connected through a network of cell walls. Due to their high rigidity, cell walls are central in plant mechanobiology. These walls must be rigid to provide strength, yet yield readily to accommodate growth (10). The mechanical modulation of cell walls within living tissues has been previously explored via live cell imaging of cellulase synthase enzymes and microtubules, to assess evolution of the spatial distribution

and amount of cellulose during development (11). Additionally, atomic force microscopy (AFM)-based imaging has been used to provide complete maps of apparent elastic modulus of cell walls (12), while Brillouin imaging was employed to measure spatial variations in extracellular matrix stiffness (13). However, methods for direct observations at high resolution are still needed. Existing methods to probe viscosity in living cells, such as fluorescence recovery after photobleaching (14–16) (FRAP) or particle-tracking microrheology (17, 18), can provide valuable insight into these phenomena but do not enable observations to be made with sufficient spatial and temporal resolution to create viscosity maps of entire tissues with subcellular resolution.

Here we describe a set of four rigidochromic molecular rotors as microviscosity probes that target the cytosol, vacuole, plasma membrane, and cell walls in plant cells and tissues. Combined with fluorescence lifetime imaging, these sensors are used to create complete microviscosity maps of individual cells or multicellular plant tissues. We employ this approach to show how apparent viscosity correlates with cell identity and function in growing roots. Moreover, we use the probes to visualize changes in cell wall flexibility during the formation of root hairs, and during the actuation of stomata.

Results

Molecular rotors are fluorescent probes that undergo an internal rotation upon photoexcitation. Conversion to this twisted state enables intramolecular charge transfer and opens a pathway of nonradiative decay for the excited state. The rate at which this

Significance

Spatial variations in microviscosity are triggered throughout plant cells, and these provide insight into local mechanobiological processes. However, it has so far been challenging to visualize such variations in living plant cells. Here we report an imaging microviscosity toolbox of chemically modified molecular rotors that yield complete microviscosity maps of several key plant cell structures. This toolbox opens up new ways to understand the role of mechanical stress in the regulation of biological processes.

rotation occurs is determined by the direct environment in which the molecular rotor is situated; molecular rotors are rigidochromic, with a fluorescence lifetime and intensity that depends on the rotational constraints imposed by their surroundings. As a result, the fluorescence lifetime provides a direct measurement of the probe rotation rate and is completely independent of the probe concentration. This rate is determined by several factors, such as hydrodynamic drag (viscosity), probe confinement, solvent polarity (19, 20), and binding. The term microviscosity refers to the apparent viscosity a simple liquid should have to give the same rotation rate. Even though it is difficult to strictly disentangle the respective effects of these factors in all cases, we can interpret the observed fluorescence lifetime patterns by taking into account the nature of the different cell compartments. For instance, lifetime fluctuations observed within the plasma membrane will not have the same implications as similar fluctuations observed in the cell wall. In the plasma membrane, a change in lifetime will reflect changes in free volume, which can be interpreted as alterations in the lipid spacing. By contrast, in the cell wall it will most likely reflect changes in the network mesh size. In the cytoplasm, the rotation rate of the probe will be mainly affected by the local crowding density, but in the noncrowded and more homogeneous environment of the vacuole, the rotor will act as a simple viscosity probe. Rigidochromic dyes have found use as microviscosity probes in polymeric materials (21), as pressure sensors in frictional contacts (22, 23), and as flow sensors in microfluidics (24). Due to their hydrophobic structure, their use in biology has so far been limited to studies of membranes in mammalian cells (25–27). To enable broad, universal use of these sensors, we use phenyl-substituted borondipyrromethene (Ph-BODIPY) molecular rotors of which the substitutions on the phenyl ring facilitate selective targeting of the different parts of the plant cell. Addition of anionic sulfonate groups (sulfo-BODIPY or sulfo-BDP in short, Fig. 1A) should facilitate diffusion across the wall and plasma membrane, and indeed results in localization into the aqueous vacuole. Functionalization of the Ph-BODIPY with a neutral poly(ethylene glycol) (PEG) chain substituent (PEG-BDP, Fig. 1B) enables passage of wall and plasma membrane but restricts entry to the vacuole, resulting in cytoplasm localization. To target the plasma membrane, we modified the phenyl ring with an aliphatic tail that carries two permanent cationic charges (26) (N$^+$-BDP, Fig. 1C). Finally, binding to the cell wall was achieved through modification of the rotor with a peptide that mimics the pectin-binding domain of Extensin proteins (28) (cell wall binding-peptide–BDP, or CWP-BDP in short, Fig. 1D). Each probe was used for plant cell staining at a concentration of 10 μM.

The localization in these different compartments is exemplified by staining suspension-cultured cells of *Arabidopsis thaliana*, as shown in Fig. 1 E–H and in *SI Appendix*, Fig. S1. We confirm the high selectivity of localization in the walls and plasma membranes in root tissues of *Arabidopsis* by means of colocalization analysis using established counterstains (*SI Appendix*, Figs. S2–S5). We show that the selectivity is retained for N$^+$-BDP when varying the probe concentration and incubation time (*SI Appendix*, Figs. S4 and S5). Using water-glycerol mixtures, we studied the response of the rotors to changes in viscosity. We find that the modified rotors exhibit a continuous increase in fluorescence lifetime with decreasing solution viscosity, and thus retain their rigidochromic properties (*SI Appendix*, Fig. S6). Importantly, we observed that the different targeting functionalities of the probes have limited effect on the fluorescence lifetime, except in the case of PEG-BDP, whose viscosity response deviates from the one of the other probes. One possible explanation for this divergence relates to the bigger volume occupied by the PEG tail compared to the other functional groups. The PEG chain could modify the environment locally probed by the rotor.

The fluorescence lifetime imaging microscopy (FLIM) microviscosity images also provide with quantitative information, which we extract as lifetime probability distributions $P(t)$. As a control, we determine the width of the lifetime distribution in pure culture medium, which gives a measure for the statistical uncertainty in our experiments. For example, the lifetime distribution in the vacuole (Fig. 1I), with sulfo-BDP, exhibits a monomodal distribution centered at 1.6 ± 0.1 ns. This is almost identical to that of the culture medium and reflects the aqueous and noncrowded nature of the vacuolar environment, with a viscosity almost identical to that of pure medium. By contrast, all other cell compartments exhibit both a significant increase in lifetime and width of the distribution, as compared to medium alone (Fig. 1 J–L). This reflects the much higher confinement and spatial inhomogeneity within the different cellular substructures.

Contrary to the noncrowded vacuoles, the cytoplasm consists of an aqueous solution crowded with a wide variety of bio(macro)molecules. Indeed, for suspension-cultured *Arabidopsis* cells, the PEG-BDP probe reveals an average lifetime of 2.6 ± 0.2 ns in the cytoplasm (Fig. 1J). Interestingly, the distribution is very wide; comparison to the control data shows that this broadening is well above the noise level of the measurements, and thus reflects the spatial inhomogeneity of the crowded cytosolic solution. Apparently, the cytoplasm undergoes large density fluctuations. The plasma membrane and tonoplast (Fig. 1K) also exhibit a broad distribution that reflects spatial inhomogeneities, as we will discuss in more detail below, with a characteristic average lifetime of 4.4 ± 0.6 ns. Finally, the broad lifetime distribution obtained with the wall-targeting rotor (Fig. 1L) reveals a strongly inhomogeneous microenvironment for the walls in cultured cells. Moreover, different wall types exhibit striking differences in their observed apparent viscosity. This will be discussed in more detail below.

After this calibration using suspension-cultured cells and cell clusters, we applied our method to 4-d-old *Arabidopsis* roots (Fig. 2 A–H and *SI Appendix*, Figs. S7 and S8). Qualitatively, the localization was equal to that in the suspension culture; we only needed to optimize the incubation times based on permeation kinetics assays (*SI Appendix*, Figs. S9–S12). For the N$^+$-BDP plasma membrane probe, the incubation time does not significantly affect the localization specificity in *Arabidopsis* roots, as can be seen in *SI Appendix*, Fig. S5. The high quantum yield of the rotors allows for the use of low laser intensities, i.e., less than 10 μW after the objective, resulting in low autofluorescence (*SI Appendix*, Fig. S13) and a high signal-to-noise ratio. Moreover, the staining is persistent over at least 5 h (*SI Appendix*, Fig. S14), indicating limited or no metabolic turnover of the dye. The vacuoles (Fig. 2 A and B) do not show any significant spatial gradients in viscosity along the root, consistent with homogeneous aqueous solutions. The other rotors, as for the suspension cells, reveal strong spatial inhomogeneities in the microviscosity of the tissue (Fig. 2 C–H). We note that internalization of the PEG-decorated cytosolic probe is weak in the root tip (Fig. 2 C and D), probably because it may adhere to the protective cuticle. During cell division and differentiation, strong changes are expected to occur primarily to the apparent viscosity of the plasma membranes and walls. For example, growth and changes in cell geometry induce localized tension on the plasma membranes (29–31) and require loosening of the cell walls to accommodate these processes (10, 32, 33). We thus focused essentially on the plasma membranes and cell walls.

The positively charged plasma membrane-targeting rotor N$^+$-BDP is designed to insert between the negatively charged phospholipids. Changes in lipid packing order and density change the volume available for the rotational motion of the probe and thus induce a change in their fluorescence lifetime. As our plasma membrane probe will sense both lipid phase transition as well as changes in local membrane tension, it becomes difficult to disentangle those two effects in a static FLIM experiment. We developed a model system to highlight the probe sensitivity to changes in lipid packing.
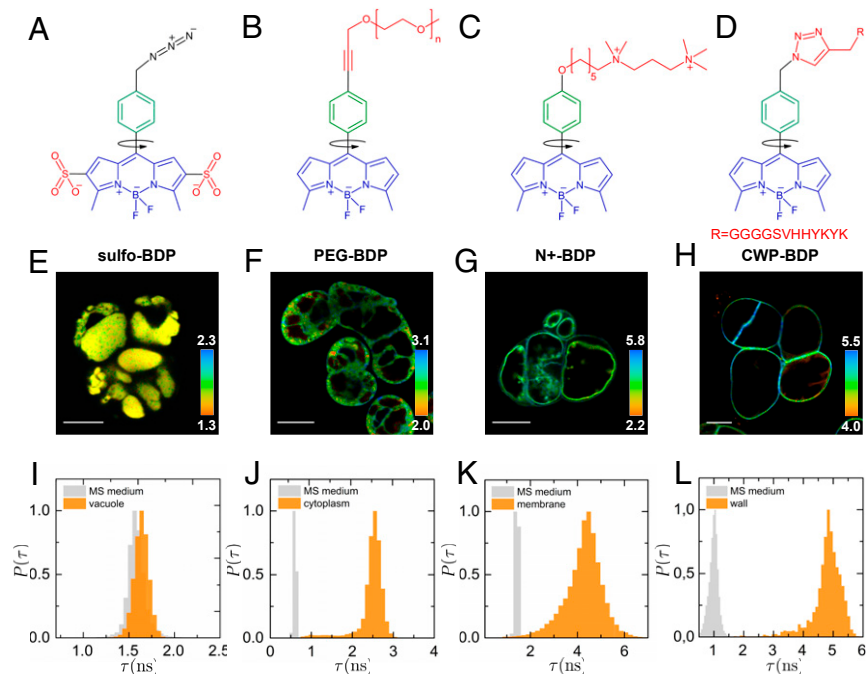
Fig. 1. Chemical structures of the four rotors (*A–D*) that target (from left to right) the vacuole, cytosol, plasma membrane, and cell wall, with (*E–H*) representative FLIM images of rotor-stained *Arabidopsis* suspension-cultured cells. (Scale bar: 20 μm.) The color scale translates the fluorescence lifetime values expressed in nanoseconds and corresponding fluorescence lifetime probability distributions (*I–L*); control measurements of fluorescence lifetime distributions are shown in gray.

Specifically, we introduced our plasma membrane probe into giant unilamellar vesicles (GUVs) composed of sphingomyelin (SM), 1,2-dioleoyl-sn-glycero-3-phosphocholine (DOPC), and cholesterol (0.56:0.24:0.20) in order to study lipid phase transition. This lipid composition leads to phase separation between a gel-like ordered (Lo) phase, rich in SM and cholesterol, and a liquid-like phase (Ld) that is enriched in DOPC. This phase separation shows similarities to the formation of lipid microdomains in biological membranes by immiscibility of different lipids (34–36). A homogeneous GUV of only DOPC shows a narrow monomodal lifetime distribution with
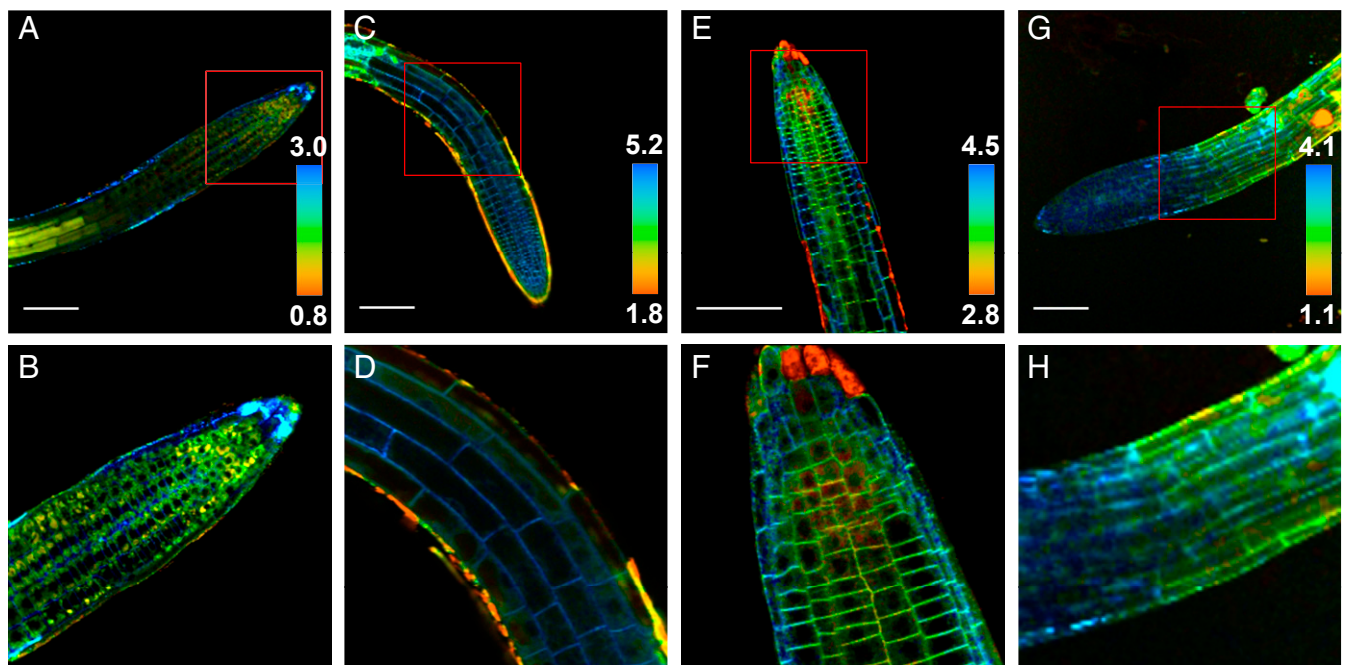
Fig. 2. Fluorescence lifetime microviscosity maps of *Arabidopsis* roots showing the vacuoles (sulfo-BDP, *A* and *B*), cytosol (PEG-BDP, *C* and *D*; note that the dye penetrates poorly in the meristem region), plasma membranes (N⁺-BDP, *E* and *F*), and cell walls (CWP-BDP, *G* and *H*), in all images. (Scale bar: 100 μm.) Red boxes in *A*, *C*, *E*, and *G* indicate close-ups shown in the *B*, *D*, *F*, and *H*, respectively.

lifetimes of 4.2 ± 0.1 ns (Fig. 3 A and C). In the mixed GUV the formation of distinct mechanical domains can be observed (Fig. 3 B and C and *SI Appendix*, Fig. S15), with lifetimes of 4.2 ± 0.4 ns in the Ld phase, which is almost identical to that measured in a pure DOPC membrane, and 5.0 ± 0.3 ns in the Lo phase. Clearly, our probe senses the stronger mechanical restriction for rotations in the tightly packed and solid-like SM-rich Lo phase. Importantly, the same rotor reveals mechanical stress on biological membranes that are exposed to external stimuli. Specifically, exposing suspension cells in their growth medium to hyperosmotic shock results in compression of the plasma membrane and concomitant reduction of the rotational motion (Fig. 3 D and E). As a consequence, lifetime distributions show a distinct shift to higher lifetimes (Fig. 3F).

When used in multicellular tissue, clear differences in microviscosity between the root cap and the meristem emerge, as seen both in the FLIM images and corresponding lifetime distributions (Fig. 3 G and H). The meristem is the tissue in plants where division of undifferentiated cells takes place. As a result of this continuous division and initial growth of the cells in the meristem, the cell plasma membranes are under constant tension. This tension, by contrast to compression that was discussed above, increases the spacing between the lipids (37) and thus leads to a distinct reduction in the membrane rotor lifetime: 4.4 ± 0.1 ns in the relaxed plasma membranes of the root cap cells and 4.2 ± 0.2 ns in the proximal (youngest part of the) root meristem. A closeup view of the plasma membranes of young epidermal cells in the meristem (Fig. 3 I and J) reveals distinct lipid microdomains within a single bilayer. Since their size is in agreement with previous findings (38), we assume that these islands where the rotor has a longer lifetime are formed by lipid compositions with higher packing density. The fact that we also observe these domains in the plasma membrane of the outermost cell layer and in suspension-cultured cells (*SI Appendix*, Fig. S16) strongly suggests that they are not plasmodesmata.

A striking example of how cellular processes control tension in the plasma membrane is found in the growth of root hairs. These are cellular protrusions that form in the differentiation zone of the root and that increase the root surface area to enhance nutrient uptake. Root hairs are commonly used as a model to study cell growth at the single cell level as they grow as fast as ~1 μm/min or more, without losing their integrity. The distinct bulging of the trichoblast cells at the initial stage of hair growth can be seen in Fig. 3 K and L. As could be expected, the lifetime is lower in the plasma membrane at the tip of the hair as compared to that of a nongrowing epidermal cell plasma membrane (Fig. 3M), shifting from 3.6 ± 0.8 ns in the hair tip to 4.3 ± 0.6 ns in nonhair epidermal cell (atrichoblast). This shift corresponds to the increased tension in the hair tip where growth occurs and curvature of the membrane is largest. A plasmolysis experiment performed on root hairs (Fig. 3 $T–Y$ and *SI Appendix*, Fig. S17) corroborated the probe responsiveness to changes in membrane tension within *Arabidopsis* root tissues. Upon hyperosmotic shock, the fluorescence lifetime within hair tip plasma membranes increases noticeably and becomes higher than within the side plasma membranes (Fig. 3Y). This change follows the drop in tension occurring upon plasmolysis, as the plasma membrane retracts and detaches from the cell wall. The same trend is observed in plasmolyzed atrichoblast cells (Fig. 3 $Q–S$ and *SI Appendix*, Fig. S18).

After having shown the level of insight that our molecular rotors provide in the dynamics of such a compact, dynamic, and fluidic cell component as the plasma membrane, we were keen to find out which light the rotors could shed on the developmental stages of the more rigid but still dynamic cell wall that is less densely packed with molecules than the plasma membrane. For this, we equipped the azide-functionalized Ph-BODIPY rotor with a pectin-binding peptide using copper-catalyzed alkyne-azide cycloadditon (CuAAC) reaction (39).

The cell wall-targeting molecular rotor binds to pectin polymers in the walls through a recognition peptide, with an amino acid sequence derived from wall binding Extensin proteins (28). Initially, a young cell has a thin and flexible primary wall that is rich in callose and contains highly methyl-esterified pectin polymers. As the cell grows, the wall is progressively consolidated by cellulose, and callose is degraded. While entering the elongation phase, the cell wall is loosened by specialized proteins, e.g., Expansins, resulting in increasing mesh size and flexibility to enable growth driven by turgor pressure. The cell wall is then stiffened by cross-linking of wall extensins. Meanwhile, the pectins are selectively deesterified, which allows them to form a gel-like matrix around the cellulose-xyloglucan network via Ca^{2+} linkages. Those dynamic changes stabilize the cell wall and result in a rigid structure with larger meshes (10, 40, 41). In mesostructured materials, such as the polymeric network of the cell wall, molecular rotors probe the local free volume rather than the viscosity of the solvent in the meshes (42). The rotation of the molecule to its twisted state sets up a hydrodynamic field of the fluid; the strength of the coupling of this field to the surrounding network determines the rotation rate. Thus, the rotor is expected to experience distinct fluorescence lifetime changes during cell wall remodelling, decreasing the lifetime as the cell wall increases its mesh size. This is exactly what we observe in suspension-cultured cells (Fig. 4 A and B). Newly formed cell-connecting walls exhibit substantially higher fluorescence lifetimes, as compared to mature walls which feature larger meshes in which the rotor can rotate more freely. Thus, this rotor enables insights into the mechanical restructuring of cell walls, upon going from flexible and compliant walls (high lifetime) to more rigid and stiff ones (low lifetime).

The cell wall-binding rotor shows weak internalization into the root apex perhaps due to the poor interaction of the rotor with the highly esterified pectins (43) (Fig. 4C). However, in the elongation (Fig. 4D) and differentiation zones (Fig. 4 E and F and *SI Appendix*, Fig. S19) the rotor is well internalized in the epidermal layer, and reveals a distinct reduction in the fluorescence lifetime in more mature tissue. This confirms the process of loosening the wall to accommodate volumetric expansion during elongation. The root epidermis in the differentiation zone (Fig. 4F) shows an increase in the fluorescence lifetime along the transverse direction, going from the outside in. This change in wall mesh structure could be related to changes in permeability, with the outer epidermal cells being the most permeable to facilitate the uptake of water and nutrients (44). To validate the use of the CWP-BDP probe in visualizing mechanical defects in biological setting, we compared its fluorescence lifetime in the walls of wild-type cotyledon pavement cells to that of pectin-impaired *qua2-1* (*quasimodo*) mutants (Fig. 5 $A–C$ and *SI Appendix*, Fig. S20). Previous studies demonstrated that the cell walls of calli in *qua* mutants show increased porosity, reflected by an increased release of cell wall material in the growth medium (45) and an increased water proton mobility within wall pores, as measured by NMR spectroscopy (46).

With our cell wall-specific probe we observe the same trend for the walls of pavement cells: the clear diminution in lifetime in mutants, that reflects an increased wall mesh size (Fig. 5C). Interestingly, this decrease in fluorescence lifetime within cell walls is accompanied by a decrease in lifetime within plasma membranes reported by N^+-BDP (Fig. 3 $N–P$ and *SI Appendix*, Fig. S21). We thereby highlight a decreased membrane tension coupled to the increased wall porosity. No such trend was evidenced when comparing walls of wild-type and *qua2-1* mutant roots (*SI Appendix*, Fig. S22). This observation is to be expected, given that cell adhesion defects are most pronounced in the shoots than in the roots of the mutant.

The mechanical maturation of walls is also seen in actively growing root hairs (Fig. 4 $G–I$). Lifetimes within the tip of root hairs are significantly higher as compared to epidermal walls that
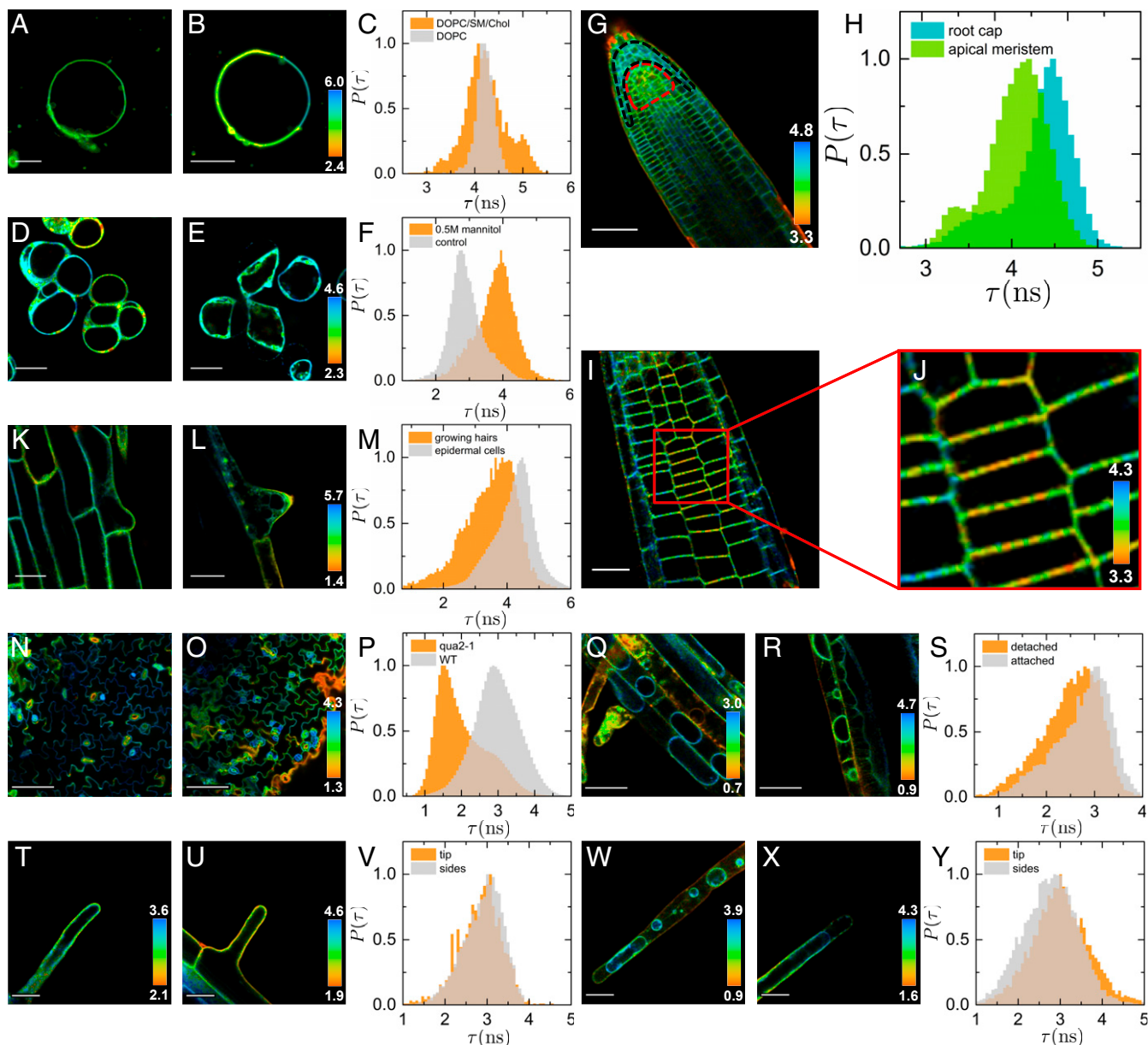
Fig. 3. Plasma membrane composition and tension imaging with N⁺-BDP. FLIM images of homogeneous DOPC GUV (*A*) and demixed DOPC/sphingomyelin/cholesterol GUVs (*B*) (Scale bars: 10 μm.) and corresponding lifetime distributions (*C*). FLIM images of *Arabidopsis* suspension-cultured cells before (*D*) and after (*E*) osmotic shock with 0.5 M mannitol to reduce plasma membrane tension (Scale bar: 20 μm.) and corresponding lifetime distributions for cells (*n* = 30) (*F*). Microviscosity maps of plasma membranes in the *Arabidopsis* root tip (*G*, Scale bar: 50 μm) and corresponding lifetime distributions (*H*) in the meristem (highlighted by a red dotted line) and in the root cap (highlighted by a black dotted line). Microviscosity maps of the root tip cortical cells (*I*, Scale bar: 20 μm), which exhibit clear mechanical microdomains in the plasma membrane (*J*, closeup view). FLIM images of growing root hairs in the maturation zone (*K* and *L*, Scale bar: 20 μm.) and corresponding lifetime distributions (*M*) in regular epidermal cells and in growing root hairs for epidermal cells (*n* = 36) and root hairs (*n* = 18). FLIM images of cotyledon pavement cells in wild type (WT) (*N*) and *qua2-1* mutant (*O*) (Scale bars: 100 μm.), and corresponding lifetime distributions (*P*) obtained for wild-type (*n* > 230) and *qua2-1* mutant (*n* > 230) pavement cells. FLIM images of root epidermal cells after plasmolysis (*Q* and *R*, Scale bar: 50 μm.) and corresponding lifetime distributions (*S*) in sections of the plasma membrane that detached from the wall versus sections of the plasma membrane still attached to the wall (*n* = 23). FLIM images of root hairs before plasmolysis (*T* and *U*, Scale bar: 20 μm.) and corresponding lifetime distributions (*V*) obtained in the tip versus the sides of the hairs (*n* = 5). FLIM images of root hairs after plasmolysis (*W* and *X*, Scale bar: 20 μm) and corresponding lifetime distributions (*Y*) obtained in the tip versus the sides of the hairs (*n* = 9).

show no root hair growth (Fig. 4*H*). In the hair tip, building blocks are secreted by exocytosis to build a new wall (47, 48). This new wall must remain compliant to accommodate further growth, and is thus composed of a primary wall enriched in a dense network of flexible pectin chains (32, 49). In addition, these root hairs must be sufficiently strong to penetrate the surrounding soil and allow water and nutrient uptake. By monitoring a young hair growth over time (Fig. 4*I*), we observe a

progressive decrease in lifetime along the hair, which reflects the same wall maturation process observed in the root itself.

Finally, we remark that spatial modulation of cell wall mechanics is not only relevant during the growth of cells or cellular protrusions, but is also key to enable the active actuation of structures in the plant. Microscopic and macroscopic motion requires the walls to be sufficiently compliant. An example of actuating organs are the stomata, pores found at the underside of
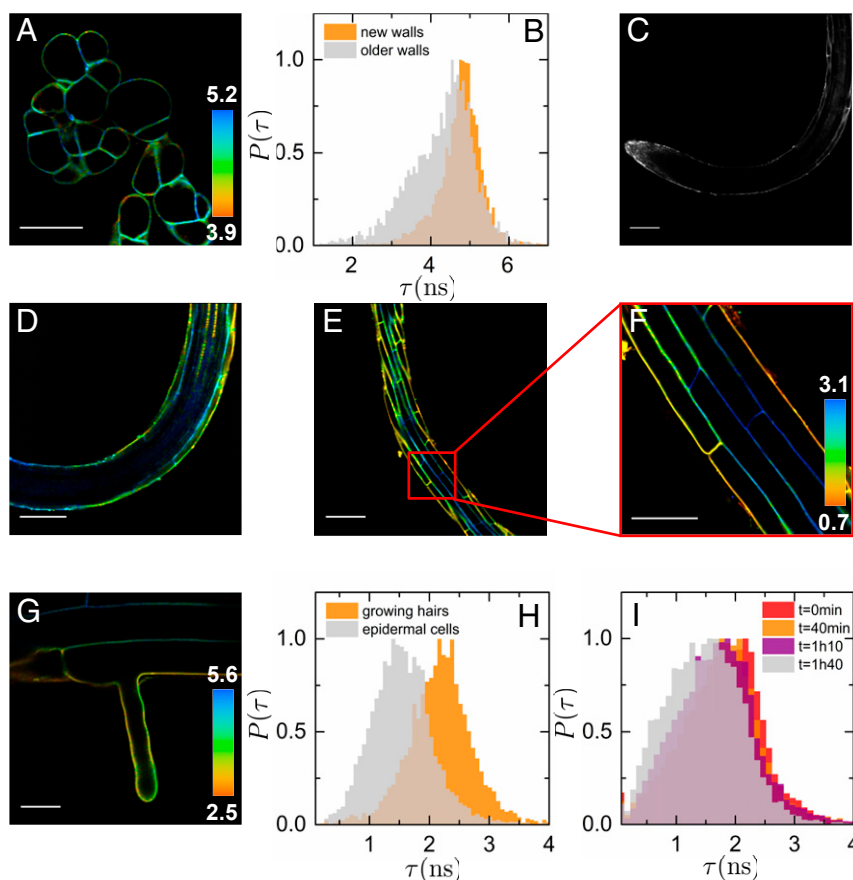
Fig. 4. Cell wall mesh size with CWP-BDP. FLIM image of *Arabidopsis* suspension-cultured cells (*A*, Scale bar: 100 μm) and corresponding lifetime distributions (*B*) in newly formed and mature walls for cells (*n* = 30). Confocal image in the *Arabidopsis* root apex (*C*, Scale bar: 100 μm). Microviscosity maps of epidermal cells in the elongation (*D*) and the maturation zone (*E*, Scale bar: 100 μm; *F*, Scale bar: 50 μm), which exhibit transverse variations in wall mesh size and compliance. FLIM images in growing root hairs (*G*) (Scale bar: 20 μm.) and corresponding lifetime distributions (*H*) in regular epidermal cells and in growing root hairs for epidermal cells (*n* = 20) and root hairs (*n* = 10). Temporal evolution of the lifetime distribution in a growing root hair (*I*).

the leaf that can be actively opened and closed to toggle gas exchange with the environment (50–52). Imaging with our cell wall-targeting rotor reveals a distinct zone of compliant wall tissue (Fig. 5 *D–F* and *SI Appendix*, Fig. S23), with a high lifetime reflecting dense pectin-rich matter (Fig. 5*F*), in the guard cells surrounding individual stoma (53). This is corroborated by the fact the fluorescence intensity is substantially higher in these areas, which indicates a higher pectin content and/or a lower pectin methylation status. Pectin deesterification has been previously correlated to wall softening in *Arabidopsis* meristem and hypocotyl (54–56). Triggering stomatal closure using an abscisic acid (ABA) treatment results in lower fluorescence lifetimes (Fig. 5 *G–I* and *SI Appendix*, Fig. S24) likely due to the induced decrease in turgor pressure. Clearly, cell wall compliance is actively regulated to match the biological function at the site of interest; our toolbox enables a direct quantification of these effects even in complex living tissues during biological function.

Discussion

We show how a set of rigidochromic molecular rotors, featuring the same mechanoresponsive core, but chemically modified to target different parts of the plant cell, can be harnessed to create complete mechanical maps of complex plant tissues. Using our tailor-made probes we have shown how the mechanics of plasma membranes and cell walls are adaptively modulated to accommodate growth or actuation. The ability to create complete time-dependent microviscosity maps of multicellular tissues, with subcellular

resolution and targeting of the key structures in the cell, opens up ways to understand the role of mechanics in the regulation of biological processes. Moreover, in combination with markers highlighting plant membrane microdomains (that remain to be identified), the plasma membrane tension probe might prove useful to study how those domains contribute to the adjustment of the plasma membrane mechanical properties. Many challenges remain in the field of plant mechanobiology, to which our approach could provide valuable insights, including the role of mechanical stress in cell polarization and differentiation, and the adaptation of local mechanics during important stages in the life cycle of the cell such as oriented division during morphogenesis. Moreover, our toolbox is not restricted to use in plants, but can be readily adapted for microviscosity mapping in multicellular tissues of other organisms, or used to probe mechanobiological phenomena in microorganisms. To bring a more quantitative assessment, more systematic studies are needed to calibrate the rotors. For instance, work on model lipid membranes to dissect the effect of membrane tension, or on synthetic polymer networks to investigate the effect of mesh confinement, would allow for quantitation of actual tensions and free volumes.

Materials and Methods

A comprehensive overview of all experimental details, including synthesis and chemical characterization of the probes, culture of the biological specimens, imaging and analysis, and statistical details for all experiments, are provided in *SI Appendix*.
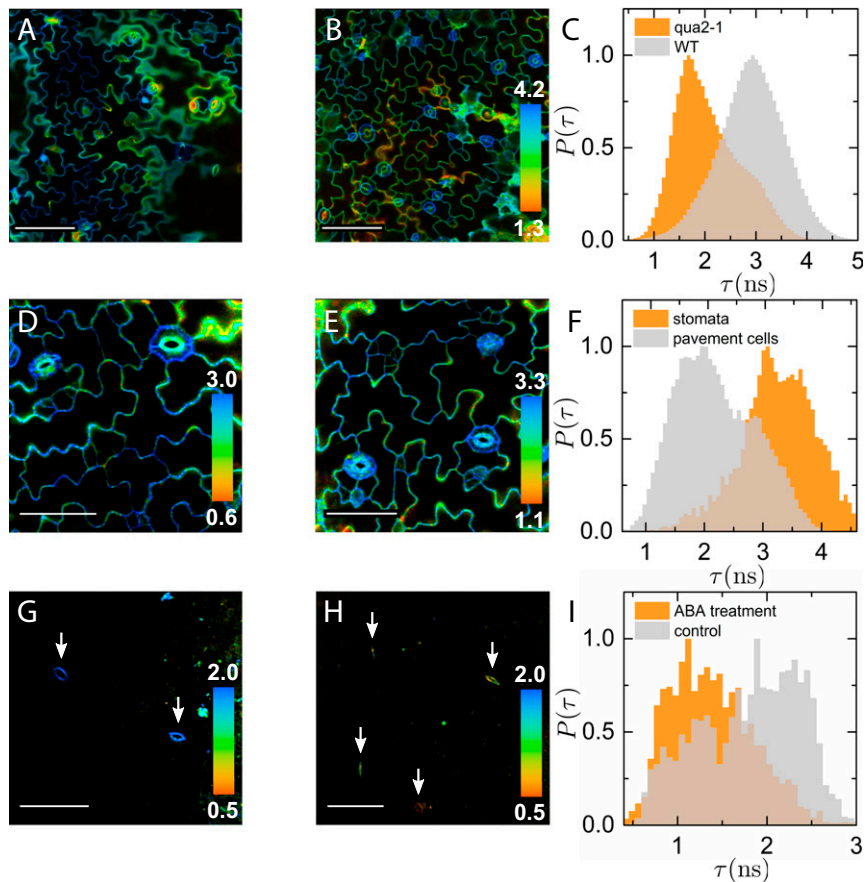
Fig. 5. Cell wall mesh size with CWP-BDP. FLIM images of cotyledon pavement cells in a wild-type (WT) *Arabidopsis* seedling (*A*) versus a *qua2-1* mutant seedling (*B*) (Scale bars: 100 µm) and corresponding lifetime distributions obtained within wild-type (*n* > 230) and *qua2-1* (*n* > 230) pavement cell walls (*C*). Zoomed in FLIM images of wild-type cotyledon epidermal layer with stomata (*D* and *E*, Scale bar: 50 µm) and corresponding lifetime distributions (*F*) for stomata (*n* = 11) in comparison with pavement cells (*n* = 15). FLIM images of cotyledon guard cells before (*G*) and after ABA treatment (*H*) (Scale bar: 50 µm), and corresponding lifetime distributions (*I*) obtained for nontreated (*n* = 13) and ABA-treated cells (*n* = 18).

Molecular Rotors. Molecular rotors were prepared by trifluoroacetic acid (TFA)-mediated condensation of 2-methylpyrrole and appropriately functionalized benzaldehydes, followed by ring closure to form the BODIPY core using boron trifluoride diethyl etherate. These basic building blocks were modified to yield the desired chemical functionality, and subsequently purified by column chromatography. Detailed procedures, yields, ^{1}H-NMR, ^{13}C-NMR, and mass spectrometry data are reported in *SI Appendix*, Figs. S25–S51. The wall-targeting peptide, inspired by the pectin-binding domain of extensin proteins (28), was prepared by Fmoc-based solid-phase peptide synthesis and attached to an azide-function rotor probe using Huisgen azide-alkyne cycloaddition (39). The peptide-functional rotor was purified using preparative reversed-phase HPLCy (high-performance liquid chromatography, HPLC). The absorption and fluorescence emission spectra of the four rotors were recorded in Milli Q water (*SI Appendix*, Figs. S52–S55), so as to determine the excitation and emission wavelengths to use for imaging.

Lifetime Calibration and Imaging. Viscosity-lifetime calibration curves were established by dissolving 10 µM of rotor dyes in water-glycerol mixtures of known viscosity. Lifetimes were recorded by time-correlated single-photon counting (TCSPC) experiments performed on an Edinburgh FS5 spectrometer, equipped with a 100-ps pulsed laser at 475 nm. In all cases, a single-exponential decay was observed in the time-resolved fluorescence measurements, from which the characteristic fluorescence lifetime was obtained. FLIM imaging experiments were performed on a Leica TCS SP8 inverted confocal microscope coupled to a Becker&Hickl TCSPC lifetime module (SPC830). Samples were excited with a 488- or 514-nm pulsed laser source (pulse duration <1 ps) and fluorescence was captured through a 63× water immersion objective (suspension-cultured cells) or a 20× water immersion objective (roots and cotyledons). Acquisition time was fixed at

120 s for each 256 × 256 pixel image. FLIM images were processed using the SPCImage 7.1 software to fit the fluorescence decay curves in each pixel with a two-component exponential decay. Images are reported in a false-color scale that represent the mean fluorescence lifetime for each pixel, expressed in nanoseconds.

Suspension-Cultured Cells. The PSB-D cells are a suspension culture of *A. thaliana,* ecotype Landsberg *erecta,* and were kindly provided by Geert de Jaeger, Ghent University, Gent, Belgium. *A. thaliana* PSB-D cells were maintained in suspension culture in a Murashige & Skoog (MS) minimal organics (MSMO) medium at 25 °C, in the dark under continuous agitation. Culture medium was replaced once a week. For imaging experiments, cells were first washed by centrifugation with fresh MSMO medium prior to incubation for 5 h in MSMO medium containing 10 µM of the rotor dye. Cells were then washed again against fresh MSMO medium and directly used for imaging. Osmotic shock experiments were performed by replacing the MSMO medium with MSMO medium containing 0.5 M mannitol as the osmotic agent and the cells observed 5 min after application of the hyperosmotic shock.

Multicellular Tissues. *A. thaliana* wild-type or *qua2-1* (*quasimodo*) mutant Col-0 seeds were surface sterilized in a bleach:ethanol solution for 8 min. They were subsequently washed twice in 70% ethanol and once in 100% ethanol. Sterilized seeds were plated on 0.5× Murashige & Skoog growth plates and vernalized at 4 °C for 24 h. They were grown vertically under long-day conditions (16 h light, 8 h dark) at 22 °C for 4 d. The 4-d-old seedlings were then transferred to 0.5× MS medium containing 10 µM of the rotor dye and incubated in constant light at 22 °C for 120, 90, 15, and 20 min for sulfo-BDP, PEG-BDP, N$^+$-BDP, and CWP-BDP, respectively. The seedlings were then washed for 30 s with fresh 0.5× MS medium and transferred onto a glass slide for FLIM imaging of the roots or cotyledons. Osmotic shock experiments were

performed by replacing the 0.5× MS medium with 0.5× MS medium containing 0.5 M mannitol as the osmotic agent and the seedlings observed within 7 to 15 min after application of the hyperosmotic shock.

To compare the mechanical properties of the plasma membrane and the cell wall within wild-type versus *qua2-1* mutant plants, 5-d-old *Arabidopsis* seedlings were incubated in 0.5× MS containing 10 μM N⁺-BDP or 10 μM CWP-BDP for 15 min. FLIM imaging of root epithelial and cotyledon pavement cells was then performed as described above.

GUV Preparation. All lipid compounds were purchased from Avanti Polar Lipids and used as is. Giant unilamellar vesicles were prepared using the method of Moscho et al. (57). In short, stock solutions of the lipids and cholesterol in chloroform were added to methanol placed in a roundbottom flask. An aqueous solution of 100 mM sucrose, containing N⁺-BDP in a molar ratio of 1:33 dye:lipids, was carefully added along the wall of the flask. The organic solvents were gently evaporated on a rotary evaporator at 40 °C and 40 rpm while gradually reducing the pressure. This resulted in the spontaneous formation of rotor-dye-labeled GUVs. The vesicles were then immobilized in a 0.5 wt/vol% agarose gel for imaging (58).

Colocalization Analysis. To confirm the selective localization of plasma membrane and cell wall probes, *Arabidopsis* seedlings, grown as described above, were incubated in medium containing both the rotor dyes at 10 μM and the counterstains propidium iodide (7) (PI) (cell wall, 10 mg/L) or 1,1′-dioctadecyl-3,3,3′,3′-tetramethylindotricarbocyanine iodide (8) (DiI-C18) (plasma membrane, 5 mg/L) for 5 min. The seedlings were then washed three times in fresh 0.5× MSMO medium and placed on a coverslip for imaging.

The plasma membrane staining specificity of N⁺-BDP was demonstrated via a colocalization analysis with a Pleckstrin homology (PH) domain specific for PI(4,5)P2, a type of plasma membrane lipid, using *pUBQ10::mCherry-1xPH(PLC)* seedlings (59).

To further study the impact of N+-BDP concentration and incubation time on the staining specificity, colocalization concentration series (1 μM, 5 μM, 10 μM, and 20 μM) and time series at 10 μM were recorded. In those series, *N*-(3-triethylammoniumpropyl)-4-(6-(4-(diethylamino) phenyl) hexatrienyl) pyridinium dibromide (FM4-64) (60) was used as counterstain to mark the plasma membrane. Internalization of FM4-64 in endomembranes was avoided by pretreating the seedlings with Brefeldin A.

Data Availability. The authors declare that all the data supporting the findings of this study are available within the paper and *SI Appendix*. Raw data and details of experimental procedures are available upon request from the corresponding authors.

1. E. O. Puchkov, Intracellular viscosity: Methods of measurement and role in metabolism. *Biochem. Moscow Suppl. Ser. A* **7**, 270–279 (2013).
2. S. Uribe, J. G. Sampedro, Measuring solution viscosity and its effect on enzyme activity. *Biol. Proced. Online* **5**, 108–115 (2003).
3. B. Gavish, M. M. Werber, Viscosity-dependent structural fluctuations in enzyme catalysis. *Biochemistry* **18**, 1269–1275 (1979).
4. J. G. Carlson, Protoplasmic viscosity changes in different regions of the grasshopper neuroblast during mitosis. *Biol. Bull.* **90**, 109–121 (1946).
5. S. W. de Laat, P. T. van der Saag, S. A. Nelemans, M. Shinitzky, Microviscosity changes during differentiation of neuroblastoma cells. *Biochim. Biophys. Acta* **509**, 188–193 (1978).
6. A. Vasanji, P. K. Ghosh, L. M. Graham, S. J. Eppell, P. L. Fox, Polarization of plasma membrane microviscosity during endothelial cell migration. *Dev. Cell* **6**, 29–41 (2004).
7. S. W. de Laat, P. T. van der Saag, M. Shinitzky, Microviscosity modulation during the cell cycle of neuroblastoma cells. *Proc. Natl. Acad. Sci. U.S.A.* **74**, 4458–4461 (1977).
8. Z. Binenbaum, E. Klyman, I. Fishov, Division-associated changes in membrane viscosity of Escherichia coli. *Biochimie* **81**, 921–929 (1999).
9. J. Ranft et al., Fluidization of tissues by cell division and apoptosis. *Proc. Natl. Acad. Sci. U.S.A.* **107**, 20863–20868 (2010).
10. M. Somssich, G. A. Khan, S. Persson, Cell wall heterogeneity in root development of Arabidopsis. *Front. Plant Sci.* **7**, 1242 (2016).
11. C. Kirchhelle, D. Garcia-Gonzalez, N. G. Irani, A. Jérusalem, I. Moore, Two mechanisms regulate directional cell growth in *Arabidopsis* lateral roots. *eLife* **8**, e47988 (2019).
12. P. Milani et al., Matching patterns of gene expression to mechanical stiffness at cell resolution through quantitative tandem epifluorescence and nanoindentation. *Plant Physiol.* **165**, 1399–1408 (2014).
13. K. Elsayad et al., Mapping the subcellular mechanical properties of live cells in tissues with fluorescence emission-Brillouin imaging. *Sci. Signal.* **9**, rs5 (2016).
14. A. Carisey, M. Stroud, R. Tsang, C. Ballestrem, Fluorescence recovery after photobleaching. *Methods Mol. Biol.* **769**, 387–402 (2011).
15. N. B. Cole et al., Diffusional mobility of Golgi proteins in membranes of living cells. *Science* **273**, 797–801 (1996).
16. S. Nehls et al., Dynamics and retention of misfolded proteins in native ER membranes. *Nat. Cell Biol.* **2**, 288–295 (2000).
17. D. Wirtz, Particle-tracking microrheology of living cells: Principles and applications. *Annu. Rev. Biophys.* **38**, 301–326 (2009).
18. J. C. Crocker, B. D. Hoffman, Multiple-particle tracking and two-point microrheology in cells. *Methods Cell Biol.* **83**, 141–178 (2007).
19. M. A. Haidekker, E. A. Theodorakis, Environment-sensitive behavior of fluorescent molecular rotors. *J. Biol. Eng.* **4**, 11 (2010).
20. A. Vyšniauskas et al., Exploring viscosity, polarity and temperature sensitivity of BODIPY-based molecular rotors. *Phys. Chem. Chem. Phys.* **19**, 25252–25259 (2017).
21. D. Wang, R. Miyamoto, Y. Shiraishi, T. Hirai, BODIPY-conjugated thermoresponsive copolymer as a fluorescent thermometer based on polymer microviscosity. *Langmuir* **25**, 13176–13182 (2009).
22. T. Suhina et al., Fluorescence microscopy visualization of contacts between objects. *Angew. Chem. Int. Ed. Engl.* **54**, 3688–3691 (2015).
23. M. A. H. Alamiry, E. Bahaidarah, A. Harriman, T. Burab, R. Ziessel, Fluorescent molecular rotors under pressure: Synergistic effects of an inert polymer. *RSC Adv.* **2**, 9851–9859 (2012).
24. M. A. Haidekker, E. A. Theodorakis, Molecular rotors'–fluorescent biosensors for viscosity and flow. *Org. Biomol. Chem.* **5**, 1669–1678 (2007).
25. M. K. Kuimova, G. Yahioglu, J. A. Levitt, K. Suhling, Molecular rotor measures viscosity of live cells via fluorescence lifetime imaging. *J. Am. Chem. Soc.* **130**, 6672–6673 (2008).
26. I. López-Duarte, T. T. Vu, M. A. Izquierdo, J. A. Bull, M. K. Kuimova, A molecular rotor for measuring viscosity in plasma membranes of live cells. *Chem. Commun.* **50**, 5282–5284 (2014).
27. S. Raut et al., A homodimeric BODIPY rotor as a fluorescent viscosity sensor for membrane-mimicking and cellular environments. *Phys. Chem. Chem. Phys.* **16**, 27037–27042 (2014).
28. A. J. MacDougall et al., The effect of peptide-pectin interactions on the gelation behaviour of a plant cell wall pectin. *Carbohydr. Res.* **335**, 115–126 (2001).
29. A. Echard, D. Burgess, The changing lipidome during cell division. *Cell* **156**, 394–395 (2014).
30. C. E. Morris, U. Homann, Cell surface area regulation and membrane tension. *J. Membr. Biol.* **179**, 79–102 (2001).
31. M. P. Sheetz, J. Dai, Modulation of membrane dynamics and cell motility by membrane tension. *Trends Cell Biol.* **6**, 85–89 (1996).
32. D. J. Cosgrove, Growth of the plant cell wall. *Nat. Rev. Mol. Cell Biol.* **6**, 850–861 (2005).
33. K. Houston, M. R. Tucker, J. Chowdhury, N. Shirley, A. Little, The plant cell wall: A complex and dynamic structure as revealed by the responses of genes under stress conditions. *Front. Plant Sci.* **7**, 984 (2016).
34. D. Lingwood, K. Simons, Lipid rafts as a membrane-organizing principle. *Science* **327**, 46–50 (2010).
35. J. R. Silvius, Role of cholesterol in lipid raft formation: Lessons from lipid model systems. *Biochim. Biophys. Acta* **1610**, 174–183 (2003).
36. D. A. Brown, E. London, Structure and function of sphingolipid- and cholesterol-rich membrane rafts. *J. Biol. Chem.* **275**, 17221–17224 (2000).
37. A. Colom et al., A fluorescent membrane tension probe. *Nat. Chem.* **10**, 1118–1125 (2018).
38. S. Mongrand, T. Stanislas, E. M. F. Bayer, J. Lherminier, F. Simon-Plas, Membrane rafts in plant cells. *Trends Plant Sci.* **15**, 656–663 (2010).
39. V. V. Rostovtsev, L. G. Green, V. V. Fokin, K. B. Sharpless, A stepwise huisgen cycloaddition process: copper(I)-catalyzed regioselective "ligation" of azides and terminal alkynes. *Angew. Chem. Int. Ed. Engl.* **41**, 2596–2599 (2002).
40. E. R. Lampugnani, G. A. Khan, M. Somssich, S. Persson, Building a plant cell wall at a glance. *J. Cell Sci.* **131**, jcs207373 (2018).
41. S. A. Braybrook, H. Jönsson, Shifting foundations: The mechanical cell wall and development. *Curr. Opin. Plant Biol.* **29**, 115–120 (2016).
42. R. O. Loutfy, Fluorescence probes for polymer free-volume. *Pure Appl. Chem.* **58**, 1239–1248 (1986).
43. W. G. Willats et al., Modulation of the degree and pattern of methyl-esterification of pectic homogalacturonan in plant cell walls. Implications for pectin methyl esterase action, matrix properties, and cell adhesion. *J. Biol. Chem.* **276**, 19404–19413 (2001).
44. M. Barberon, N. Geldner, Radial transport of nutrients: The plant root as a polarized epithelium. *Plant Physiol.* **166**, 528–537 (2014).
45. C. Rondeau-Mouro, D. Defer, E. Leboeuf, M. Lahaye, Assessment of cell wall porosity in Arabidopsis thaliana by NMR spectroscopy. *Int. J. Biol. Macromol.* **42**, 83–92 (2008).
46. E. Leboeuf, F. Guillon, S. Thoiron, M. Lahaye, Biochemical and immunohistochemical analysis of pectic polysaccharides in the cell walls of Arabidopsis mutant QUASIMODO 1 suspension-cultured cells: Implications for cell adhesion. *J. Exp. Bot.* **56**, 3171–3182 (2005).
47. C. Grierson, Root hairs. *Arabidopsis Book* **12**, 85–102 (2010).
48. T. Ketelaar, M. E. Galway, B. M. Mulder, A. M. C. Emons, Rates of exocytosis and endocytosis in Arabidopsis root hairs and pollen tubes. *J. Microsc.* **231**, 265–273 (2008).
49. R. Palin, A. Geitmann, The role of pectin in plant morphogenesis. *Biosystems* **109**, 397–402 (2012).

50. A. M. Hetherington, F. I. Woodward, The role of stomata in sensing and driving environmental change. *Nature* **424**, 901–908 (2003).
51. Z. Marom, I. Shtein, B. Bar-On, Stomatal opening: The role of cell-wall mechanical anisotropy and its analytical relations to the bio-composite characteristics. *Front. Plant Sci.* **8**, 2061 (2017).
52. P. J. Franks, G. D. Farquhar, The mechanical diversity of stomata and its significance in gas-exchange control. *Plant Physiol.* **143**, 78–87 (2007).
53. I. Shtein *et al.*, Stomatal cell wall composition: Distinctive structural patterns associated with different phylogenetic groups. *Ann. Bot.* **119**, 1021–1033 (2017).
54. A. Peaucelle, R. Wightman, H. Höfte, The control of growth symmetry breaking in the Arabidopsis hypocotyl. *Curr. Biol.* **25**, 1746–1752 (2015).
55. S. A. Braybrook, A. Peaucelle, Mechano-chemical aspects of organ formation in Arabidopsis thaliana: The relationship between auxin and pectin. *PLoS One* **8**, e57813 (2013).
56. A. Peaucelle *et al.*, Pectin-induced changes in cell wall mechanics underlie organ initiation in Arabidopsis. *Curr. Biol.* **21**, 1720–1726 (2011).
57. A. Moscho, O. Orwar, D. T. Chiu, B. P. Modi, R. N. Zare, Rapid preparation of giant unilamellar vesicles. *Proc. Natl. Acad. Sci. U.S.A.* **93**, 11443–11447 (1996).
58. R. B. Lira, J. Steinkühler, R. L. Knorr, R. Dimova, K. A. Riske, Posing for a picture: Vesicle immobilization in agarose gel. *Sci. Rep.* **6**, 25254 (2016).
59. M. L. A. Simon *et al.*, A multi-colour/multi-affinity marker set to visualize phosphoinositide dynamics in Arabidopsis. *Plant J.* **77**, 322–337 (2014).
60. S. Bolte *et al.*, FM-dyes as experimental probes for dissecting vesicle trafficking in living plant cells. *J. Microsc.* **214**, 159–173 (2004).